nature climate change

Article

https://doi.org/10.1038/s41558-024-02074-3

Reduced Arctic Ocean CO_2 uptake due to coastal permafrost erosion

Received: 16 October 2023

Accepted: 24 June 2024

Published online: 12 August 2024

Check for updates

David M. Nielsen[1,2] ✉, Fatemeh Chegini[1,2], Joeran Maerz[1,5], Sebastian Brune[2], Moritz Mathis[3], Mikhail Dobrynin[4], Johanna Baehr[2], Victor Brovkin[1,2] & Tatiana Ilyina[1,2,3]

Arctic coastal permafrost erosion is projected to increase by a factor of 2–3 by 2100. However, organic matter fluxes from the coastal permafrost into the ocean have not been considered in Earth system models so far. Here we represent coastal permafrost erosion in an Earth system model and perform simulations with varying permafrost organic matter properties, such as sinking fraction and nutrient content. We find that coastal erosion reduces the Arctic Ocean CO_2 uptake from the atmosphere in all simulations: by 4.6–13.2 TgC yr^{-1} by 2100, which is ~7–14% of the Inner Arctic Ocean uptake. We show that coastal permafrost erosion exerts a positive biogeochemical feedback on climate, increasing atmospheric CO_2 by 1–2 TgC yr^{-1} per °C of increase in global surface air temperature. Our work will allow coastal permafrost erosion to be considered in future climate change assessments.

The Arctic is the most sensitive region to anthropogenic climate change on Earth, currently warming about four times faster than the globe[1,2]. The coastal permafrost region is especially vulnerable. While increasing temperatures thaw and destabilize the ice-rich coastal permafrost[3,4], melting sea ice allows ocean-surface waves to abrade the coast[4–6]. The coastal permafrost currently erodes at a rate of 0.5 m yr^{-1} (ref. 7) and delivers organic carbon (OC) to the ocean at amounts comparable to those of all Arctic rivers combined (5–18 TgC yr^{-1} from erosion[8–10], 25–40 TgC yr^{-1} from rivers[9,11,12]), potentially increasing atmospheric CO_2 concentrations[13–16]. Observations show that erosion has accelerated throughout the Arctic[17–20], and the Arctic-mean erosion rate is projected to increase by a factor of 2–3 by the end of this century[21]. However, Earth system models (ESMs) so far have not considered organic matter (OM) fluxes from coastal permafrost into the ocean. Therefore, projected impacts of increasing coastal permafrost erosion on the Arctic carbon cycle and climate are elusive. Here we represent OM fluxes from coastal permafrost erosion in the Max Planck Institute Earth system model (MPI-ESM)[22] and investigate the ocean's biogeochemistry response. We assess the impact of coastal permafrost erosion on the Arctic Ocean's uptake of atmospheric CO_2 until the end of this century and explore the underlying mechanisms.

More than 90% of the ocean uptake of atmospheric CO_2 occurs in polar and subpolar regions[23]. Over the Arctic shelves, CO_2 uptake is estimated at ~70 TgC yr^{-1}, among the largest per unit area in the globe[24]. However, the sensitivity of the ocean CO_2 uptake to coastal permafrost erosion is uncertain, especially as climate change progresses into the future. Once eroded, the OC can take several paths, which differ substantially in terms of their effect on the ocean's CO_2 sink. The eroded OM may: (1) be remineralized (that is, degraded to inorganic carbon), increasing the ocean partial pressure of CO_2 (pCO_2)[14,15], (2) boost primary production, decreasing ocean pCO_2[25] or (3) settle down and be buried in the ocean sediment where remineralization is slower than in the water column[26,27]. Sediment resuspension thus plays an important role in prolonging the lifetime of the eroded OM in the water column[28]. Moreover, remineralization rates depend on OM properties, such as origin and mineral association[29,30]. The interplay among the aforementioned processes in a changing Arctic Ocean background[31,32] will determine the net impact of increasing coastal permafrost erosion on the Arctic Ocean CO_2 sink capacity.

We perform sensitivity simulations to provide uncertainty ranges due to varying permafrost OM characteristics. By using MPI-ESM, we are bounded by model limitations, such as the lacking direct

[1]Max Planck Institute for Meteorology, Hamburg, Germany. [2]Center for Earth System Research and Sustainability (CEN), Universität Hamburg, Hamburg, Germany. [3]Helmholtz-Zentrum Hereon, Geesthacht, Germany. [4]Deutscher Wetterdienst (DWD), Hamburg, Germany. [5]Present address: University of Bergen and Bjerknes Centre for Climate Research, Bergen, Norway. ✉e-mail: david.nielsen@mpimet.mpg.de

https://doi.org/10.1038/s41558-024-02074-3

representation of ocean-surface waves and their impact on sediment resuspension (see Methods for more details on model limitations). We represent variations in the primary production response to erosion by varying carbon-to-nutrient ratios (C/N ratios) in accordance with permafrost observations. We also represent variations in settling speeds by fractioning the OC flux between sinking particulate OC (POC), and low-density neutrally buoyant POC (Table 1). We use a dissolved OC (DOC) tracer to represent the latter, taking advantage of DOC's property of being passively transported without sinking in MPI-ESM. We thus represent the eroded OM as mostly sinking POC (90% POC and 10% DOC), or as mostly neutrally buoyant POC (10% POC and 90% DOC). We cover the historical period (1850–2014) and a wide range of future scenarios (2015–2100, see Methods) following the Coupled Model Intercomparison Project phase 6 (CMIP6)[33,34]. Modern ESMs do not consider abrupt permafrost degradation, whose climatic impact remains uncertain[35–37]. We take a step towards addressing this pressing need by examining specifically coastal permafrost erosion for the first time with an ESM at climatic scales.

Table 1 | Summary of sensitivity experiments including coastal erosion, where permafrost OM characteristics are changed, namely, POC–DOC fractions and C/N ratios

Experiment name	POC fraction (sinking permafrost POC) (%)	DOC fraction (buoyant permafrost POC) (%)	C/N ratio
90%POC 18C/N	90	10	18.0
90%POC 14C/N	90	10	14.0
90%POC 10C/N	90	10	10.0
10%POC 18C/N	10	90	18.0
10%POC 14C/N	10	90	14.0
10%POC 10C/N	10	90	10.0
90%POC Marine	90	10	7.6 (Redfield)
10%POC Marine	10	90	7.6 (Redfield)
Reference	MPI-ESM CMIP6 simulation without coastal permafrost erosion		

Weakening the Arctic Ocean CO_2 uptake

Coastal permafrost erosion reduces the Arctic Ocean CO_2 uptake from the atmosphere in all sensitivity simulations and scenarios (Fig. 1a). The CO_2 uptake is reduced by 2.5–5.2 TgC yr^{-1} (5–95th percentile range) in the historical period (1850–1900 mean) in comparison with the CMIP6 reference without erosion. Erosion reduces the CO_2 uptake further in the future in response to increasing anthropogenic emissions: by between 4.6–9.2 TgC yr^{-1} in Shared Socioeconomic Pathways (SSP)1–2.6 and 6.6–13.2 TgC yr^{-1} in SSP5–8.5 by the end of the century (2081–2100 mean). The CO_2 uptake reduction represents 9–19% of the total Inner Arctic Ocean CO_2 uptake in the historical period, and 7–14% of the Inner Arctic Ocean CO_2 uptake by 2100 in SSP5–8.5. In the future, the 'total' CO_2 uptake by the Arctic Ocean (as opposed to only changes due to erosion) increases with anthropogenic emissions (Fig. 1b) mainly due to decreasing sea-ice cover (Fig. 1c) and increasing atmospheric pCO_2 (despite a decrease in uptake efficiency due to warming and freshening[24,32,38]). Therefore, while coastal erosion increases, and weakens the Arctic Ocean CO_2 uptake more strongly in the future, percentage changes due to erosion are smaller in the future than historically (Fig. 1d).

The sensitivity of CO_2 uptake to coastal erosion depends mostly on how permafrost OM is represented in the MPI-ESM (Fig. 1e). The largest impact is produced in simulations with nutrient-poor (high C/N) and low-density (mostly buoyant) OM, and vice versa. One TgC released by coastal erosion (TgC_{eros}) decreases the Arctic Ocean CO_2 uptake by 0.23–0.49 TgC ($TgC_{\Delta FCO_2}$) in the simulation with mostly sinking and nutrient-rich permafrost OM (90%POC, C/N = 10), and by 0.49–1.02 TgC in the simulation with mostly buoyant and nutrient-poor permafrost OM (10%POC, C/N = 18). That is, between about one-fourth and up to all of the OC from erosion would escape to the atmosphere as CO_2, depending on permafrost OM characteristics. Relative to the total CO_2 uptake (Fig. 1d), coastal erosion reduces the Inner Arctic Ocean CO_2 uptake by between 6–8% (90%POC, C/N = 10) and 14–19% (10%POC, C/N = 18). Our sensitivity simulations thus produce large uncertainties, comparable to those estimated from observations.

Early observational estimates proposed that ~66% of the OC from erosion would escape to the atmosphere as CO_2 (ref. 14), while the remainder would settle in the sediment (see supplementary text on 'POC export and sedimentation fluxes'). However, recent incubation experiments of permafrost in seawater pointed to substantially lower CO_2 production: up to ~5–6% of the eroded OC after 4 months (approximately one ice-free season) at 4 °C[15,16], ~13% after 4 months at 16 °C[15], and ~34% and 41% of OC loss after 14 and 28 days, respectively, at 20 °C[39]. Ship measurements estimated terrestrial POC and DOC loss fractions at ~1.4 and 0.3 yr^{-1}, respectively[40,41]. Such observational OC loss estimates translate to linear remineralization rates ranging from $\mathcal{O}(10^{-4})$ to $\mathcal{O}(10^{-2})day^{-1}$. Variability in remineralization rates depends on several factors, such as temperature, erosion type and transport time (for example, cliff undercutting and sudden collapse versus thaw slumping[15,16]), and organo-mineral interactions[30]. Although the representation of OM remineralization dynamics has been recently improved in global models[42,43], these dynamics do not yet consider permafrost OM specifically and have not been considered in future climate simulations so far. In this version of MPI-ESM, OM remineralization rates are fixed globally at 2.6×10^{-2} and 8.0×10^{-3} day^{-1} for POC and DOC, respectively[42,44]. This simplification poses limitations to the interpretation of our results, especially in absolute terms, as we do not estimate uncertainties due to varying remineralization rates. We continue to investigate the spatiotemporal variability and the mechanisms underlying the reduction in the Arctic Ocean CO_2 sink in response to coastal permafrost erosion.

Regional shifts in CO_2 sinks and sources

The largest reduction in CO_2 uptake is simulated in the Laptev and East Siberian Seas (LESS), where the yearly net CO_2 flux direction is inverted due to erosion. The LESS shelves act as a CO_2 sink in the reference MPI-ESM simulation from CMIP6, and as a net CO_2 source in all simulations with coastal permafrost erosion. Such inversion is simulated both at present-climate conditions (Fig. 2a,b) and in future emission scenarios (Extended Data Fig. 1), and in all sensitivity simulations, as a response to the disproportionately large OC flux from erosion. The LESS alone receives about three-quarters of the pan-Arctic OC flux from erosion, also both at present[10] and in future scenarios[21]. Our simulated CO_2 outgassing in the LESS is in agreement with several observations made in the past two decades[13,45–50].

Observations have long shown that the degradation of terrestrial OM delivered by coastal erosion increases surface pCO_2 in the LESS[51] which, in turn, decreases the ocean CO_2 sink. An east–west gradient in pCO_2 has been observed in the LESS[46–49], which is also captured in our simulations. On the one hand, surface pCO_2 is relatively high in the vicinity of the Lena River delta and the highly erosive Muostakh Island and Buor-Khaya Bay regions (~130° E), where episodic outgassing CO_2 fluxes range in the order of 1–100 mgC m^{-2} day^{-1} (refs. 48,49). On the other hand, surface pCO_2 decreases towards the east, with decreasing influence of terrestrial inputs and increasing influence of Pacific water masses, where CO_2 is conversely taken up by the ocean[45–47]. As a second-order control, temperature and atmospheric circulation also determine the strength and interannual variability of the CO_2 flux gradient[46,48]. Such gradient has also been verified in patterns of ocean acidification, which increases in response to increasing pCO_2 (ref. 50). In fact, the degradation of terrestrial OM delivered by coastal erosion and

https://doi.org/10.1038/s41558-024-02074-3

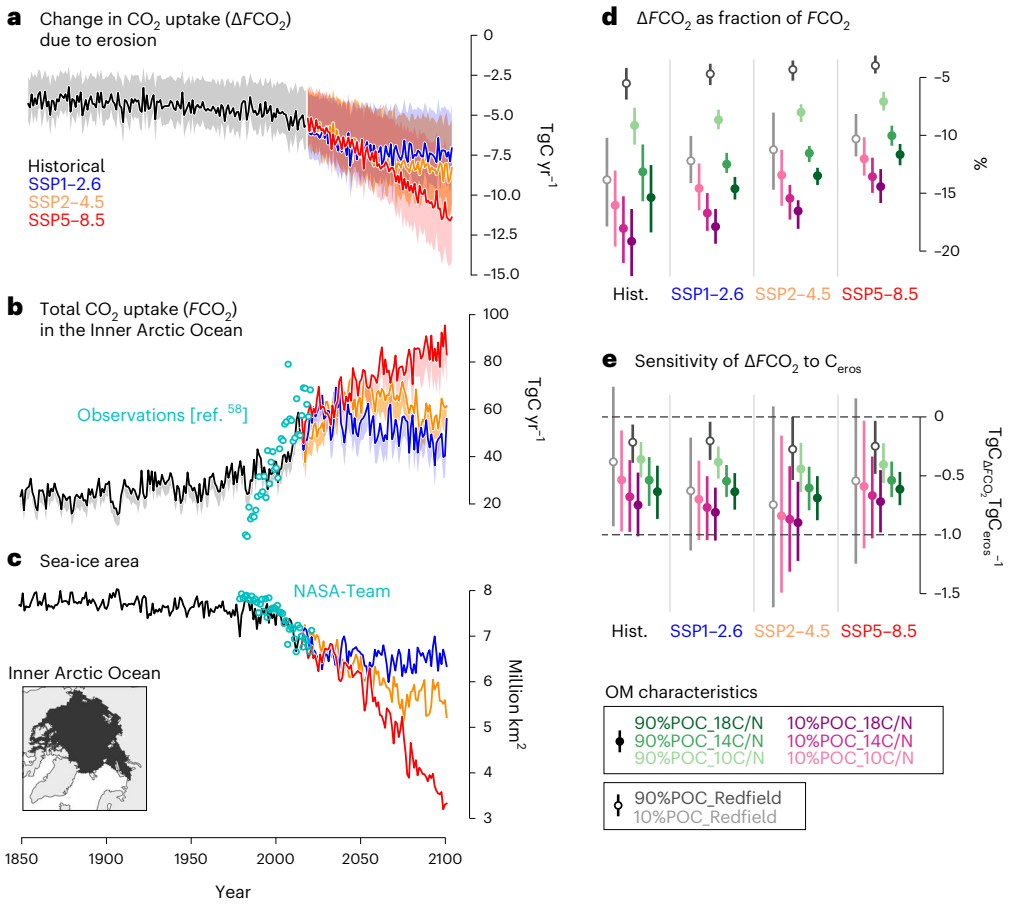

Fig. 1 | Changes in CO_2 uptake due to erosion. a, Annual changes in the Arctic Ocean's uptake of atmospheric CO_2 due to coastal permafrost erosion. The shading represents the range of uncertainty stemming from varying OM permafrost characteristics in our simulations, while the solid line represents the mean response. **b**, Total Inner Arctic Ocean CO_2 uptake without coastal erosion (lines) and with coastal erosion (shade). **c**, Evolution of the Inner Arctic Ocean's sea-ice area. **d**, Change in CO_2 uptake due to erosion as percentage of the total Inner Arctic Ocean uptake. **e**, Sensitivity of change in CO_2 uptake (in mass of carbon) due to erosion per unit mass of OC from erosion. In **d** and **e**, temporal means are taken over the historical period (1850–1900) and over the last 20 years of the future scenarios (2081–2100). Vertical bars depict the 5–95th percentile range of the yearly values of the mean in **d**, and the 5–95th percentile range of the regression coefficient estimates in **e** (Methods). We integrate the ocean CO_2 uptake in the Inner Arctic Ocean domain (inset in **c**), which excludes regions of strong Atlantic influence and perennial open water (for example, parts of Barents, Greenland and Norwegian Seas), and little erosion[7].

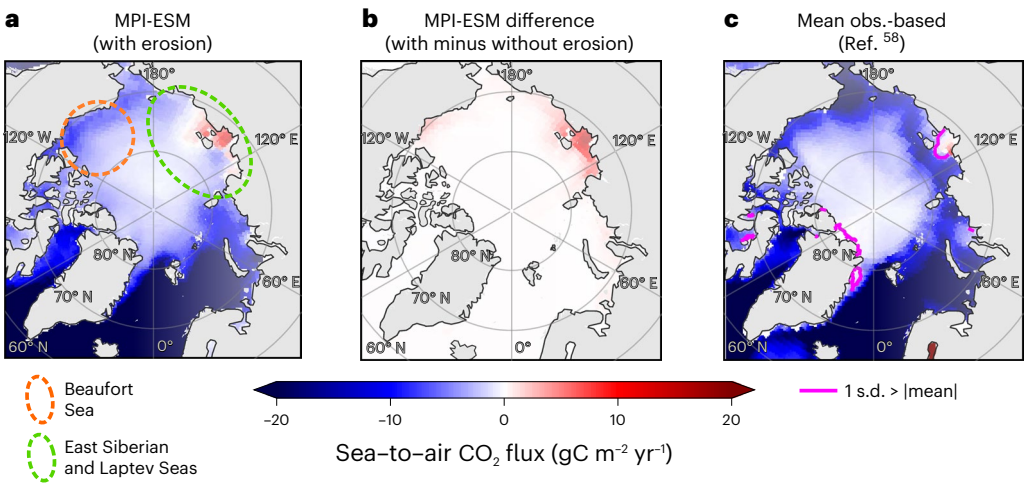

Fig. 2 | Spatial patterns of CO_2 flux. a, Air–sea CO_2 fluxes in SSP2–4.5 averaged over all simulations with permafrost OM erosion (first 6 simulations in Table 1). **b**, The difference with respect to the CMIP6 reference without erosion. **c**, Mean observations-based neural-network CO_2 flux estimate from ref. 58. Regions where the interannual variability (expressed as 1 s.d.) is larger than the mean's magnitude are contoured in pink in **c**, highlighting the Laptev Sea coastal shelf region. All statistics are over the 1991–2010 period.

https://doi.org/10.1038/s41558-024-02074-3

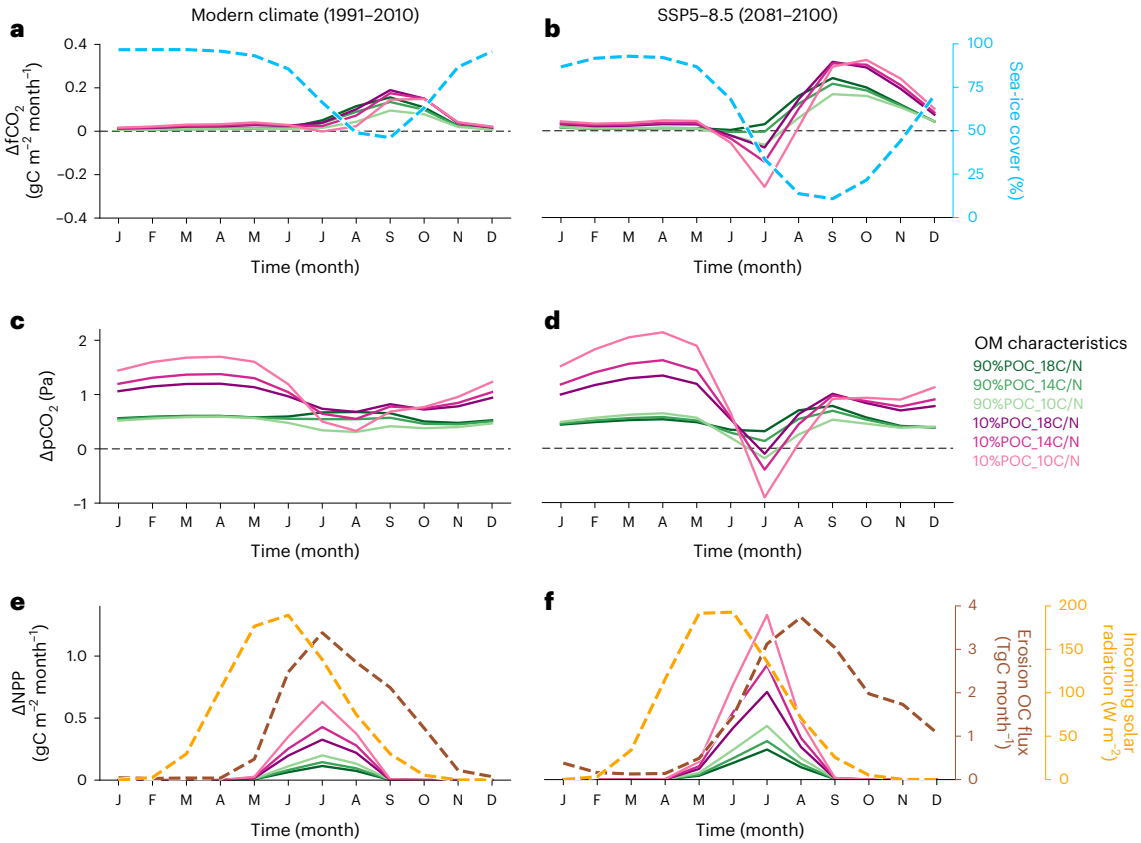

Fig. 3 | Seasonal cycle of changes due to erosion. a,**b**, CO_2 flux anomalies and sea-ice concentration averaged over the Inner Arctic Ocean domain for the modern-climate period (1991–2010) (**a**) and end-of-century period in SSP5–8.5 scenario (2081–2100) (**b**). **c**,**d**, Surface partial pressure of CO_2 anomalies for the modern-climate (**c**) and SSP5–8.5 (**d**) scenarios. **e**,**f**, NPP anomalies for the modern-climate (**e**) and SSP5–8.5 (**f**) scenarios, together with OC fluxes from coastal permafrost erosion and incoming shortwave radiation at the surface. All anomalies are changes due to permafrost erosion (with respect to CMIP6 reference without erosion). Other future scenarios show qualitatively similar anomaly patterns to that of SSP5–8.5, but with smaller magnitudes.

rivers is shown to be the main driver of ocean acidification in the LESS, as opposed to increasing anthropogenic atmospheric CO_2 uptake[50].

Parallel to coastal erosion, the role of rivers in driving CO_2 outgassing over the LESS shelves has also been observed and reproduced with models[46,52–56]. In the Beaufort Sea, rivers drive CO_2 outgassing in the nearshore zone[57], especially in years of strong discharge[56]. Riverine fluxes shift the yearly mean CO_2 flux directions in the Laptev and Beaufort Seas from net sinks to net sources in historical simulations performed with a previous version of MPI-ESM[55]. In our simulations, the impact of erosion is comparatively small in the Beaufort Sea. The OC flux delivered by erosion in the Beaufort Sea is about one-tenth of that delivered by rivers[9], and about one-fifth of that delivered by erosion in the LESS[10,21].

Observations-based global CO_2 flux products suggest that the LESS shelves are spatially heterogeneous and variable in time, acting both as sink and as source of CO_2 at different times[58,59]. The southern Laptev Sea would act as net source of CO_2 at modern-climate conditions (1991–2010), while it is among the few Arctic shelf regions where the estimated interannual standard deviation is larger than the climatological mean (Fig. 2c,d), highlighting the large variability and suggesting a strong local response to coastal erosion and riverine fluxes.

Changes at the seasonal scale

Changes in air–sea CO_2 fluxes due to erosion are inversely proportional to sea-ice cover at modern-climate conditions (Fig. 3a). CO_2 flux anomalies are minor until sea-ice melt starts, peak at sea-ice minimum around September, and decrease again at sea-ice freeze-up. Once more, simulations with low-POC fraction and high C/N ratio yield the largest CO_2 flux anomalies. The role of the low-POC fraction in increasing the OM residence time in the water column is evidenced by winter maximum surface pCO_2 anomalies before sea-ice melt due to continuous OM remineralization (Fig. 3c). Conversely, high-POC erosion yields a relatively constant increase in pCO_2 throughout the year. The summer months (June–July–August, JJA) are marked by an increase in net primary production (NPP) due to erosion, fuelled by the higher nutrient availability, once the eroded OM is remineralized. The increase in NPP thus peaks with OC fluxes from erosion in July, allowed by abundant sunlight (Fig. 3e). Surface pCO_2 decreases in JJA in response to positive CO_2 flux anomalies and to increasing NPP. The pCO_2 summer low is larger in simulations with 10% POC and low C/N ratios, where the NPP-consumption of dissolved inorganic carbon (DIC) is also large, while being smaller or almost absent in 90% POC and C/N = 18 simulations, where permafrost OM is poor in nutrients and short-lived in the water column.

As climate change progresses in the future, the seasonal cycle of CO_2 flux shows two distinct responses to erosion: an early increase and a later decrease in CO_2 uptake. The longer ice-free season by the end of the century in SSP5–8.5 allows for an earlier onset and a 2-fold stronger peak in NPP due to erosion in July (Fig. 3f). OM remineralization provides nutrients, which induce an early strong NPP boost causing negative pCO_2 anomalies especially in simulations with buoyant permafrost OM (see Methods for details, Fig. 3d), which translates into an early increase in CO_2 uptake during summer (Fig. 3b). While the boost in NPP ceases with decreasing sunlight, the ice-free season and thus also the OM fluxes from erosion extend longer into fall. Without CO_2 uptake by NPP, permafrost OM remineralization increases pCO_2

https://doi.org/10.1038/s41558-024-02074-3

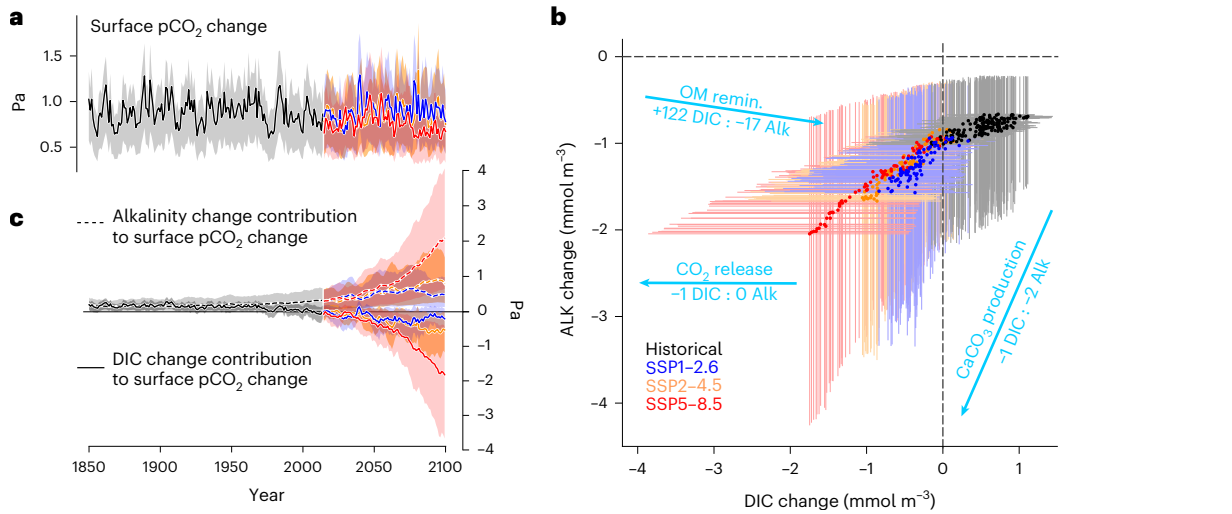

Fig. 4 | Mechanisms sustaining a surface pCO_2 increase. a–c, Anomalies in surface pCO_2 due to coastal erosion (**a**) (with respect to the reference simulation without coastal erosion) and its decomposition between the contributions from alkalinity and DIC (**c**). Anomalies in alkalinity and DIC due to coastal erosion (**b**) in comparison to the directions (ratios) of anomalies resulting from photosynthesis, air–sea exchange and $CaCO_3$ production are indicated by the arrows in **b**. The vertical and horizontal lines in **b** represent the range of uncertainty originating in different permafrost OM characteristics.

anomalies back to positive values, which switches air–sea CO_2 flux anomalies back to positive values for the rest of the year. Since the later decrease in CO_2 uptake is larger in magnitude than the summer increase, annual values are always positive, that is, yielding a yearly net decrease in the Arctic Ocean CO_2 uptake. In absolute terms, future Arctic surface pCO_2 is projected to decrease in early-spring/summer due to earlier onsets of NPP[60,61], and increase between late-summer and fall due to warming[60]. Coastal permafrost erosion would thus exacerbate this effect.

Mechanisms increasing surface pCO_2

Coastal permafrost erosion increases Arctic surface pCO_2 in all sensitivity simulations and emission scenarios. The pCO_2 increase is relatively constant in time [0.9 (0.7–1.3) Pa], and no significant differences are discernible in yearly means among future scenarios (Fig. 4a). We decompose changes in surface pCO_2 between contributions from changes in DIC and alkalinity (see Methods) to disentangle the underlying mechanisms. On the one hand, coastal erosion decreases alkalinity in all years and all simulations (Fig. 4b) due to the remineralization of OM, and due to an increase in calcium carbonate production (see Supplementary Information for details on $CaCO_3$) following an increase in primary productivity. On the other hand, the remineralization of the eroded OM initially increases DIC with respect to the simulation without coastal erosion (Fig. 4b). The continuous decrease in alkalinity, which decreases the ocean's ability to uptake CO_2 from the atmosphere, together with the steady increase in primary production, causes a steady decrease in surface DIC with time (Fig. 4b). Consequently, erosion causes net negative surface DIC anomalies in the twenty-first century, despite the DIC added by the remineralization of permafrost OM.

While changes in both DIC and alkalinity increase surface pCO_2 in the historical period, they emerge as competing mechanisms in the twenty-first century. In the historical period, both higher surface DIC and lower alkalinity contribute to increase surface pCO_2 during most of the twentieth century until the 1980s (Fig. 4c). Thereafter, changes in DIC due to coastal erosion become negative (with respect to the simulation without erosion), shifting the role of DIC in its contribution to changes in surface pCO_2 due to erosion (from positive to negative contributions). By the end of the twenty-first century, the large alkalinity decrease is followed by an also large DIC decrease (Fig. 4b). The individual contributions from DIC and alkalinity to the change in surface pCO_2 are 2 to 5 times larger than the net result by 2100 (Fig. 4c). The always slightly larger contribution from decreasing alkalinity (increasing pCO_2) than that from decreasing DIC (decreasing pCO_2) sustains the constant increase in surface pCO_2 in the twenty-first century.

The important role of terrestrial OM degradation in decreasing alkalinity in highly erosive coastal regions, and thus increasing pCO_2, is supported by extensive in situ observations[49,50,62]. The combined effect of increasing terrestrial OM degradation[50] and melting sea ice[63] will therefore accelerate acidification of the Arctic Ocean, impacting calcifying organisms and the marine ecosystem.

While the increase in surface pCO_2 due to coastal erosion does not change significantly with time (Fig. 4a), the decrease in the Arctic Ocean CO_2 uptake does (Fig. 1a). The explanation for such apparent disparity lies on sea ice. Sea ice mediates the impact of the increasing surface pCO_2 due to erosion on the changes in the Arctic Ocean CO_2 uptake from the atmosphere.

The erosion–climate feedback is mediated by sea ice

The increase in surface pCO_2 due to coastal erosion can only have an impact on air–sea CO_2 fluxes in the absence of sea ice. Therefore, the reduction in CO_2 uptake due to erosion is proportional to the Arctic-mean open-water season (OWS) duration in all scenarios and sensitivity simulations (Fig. 5a). The effect of sea ice in mediating the CO_2 uptake reduction increases with growing emissions and could account for as much as 60% of the reduced CO_2 uptake due to erosion by 2100 in SSP5–8.5 in comparison with pre-industrial times (Extended Data Fig. 2). CO_2 fluxes scale linearly with sea-ice fraction in observations[64,65] and in MPI-ESM, that is, a grid cell with 100% sea-ice concentration is totally impermeable to gas transfer. We quantify the OWS duration as the number of days per year during which sea-ice concentration is less than 15% at each model grid cell. Thus, the Arctic-mean OWS duration expresses both spatial and temporal roles of sea-ice cover in limiting air–sea CO_2 exchange in one quantity per year.

While the OWS duration mediates the CO_2 uptake response to erosion, the rate at which the CO_2 uptake is reduced per open-water day (that is, sensitivity to OW-day) again depends mainly on how permafrost OM is represented in our model. The sensitivity of the erosion-driven change in CO_2 uptake to OWS duration ranges from −0.028 TgC OW-day^{-1} to −0.054 TgC OW-day^{-1} in simulations with 90%

https://doi.org/10.1038/s41558-024-02074-3

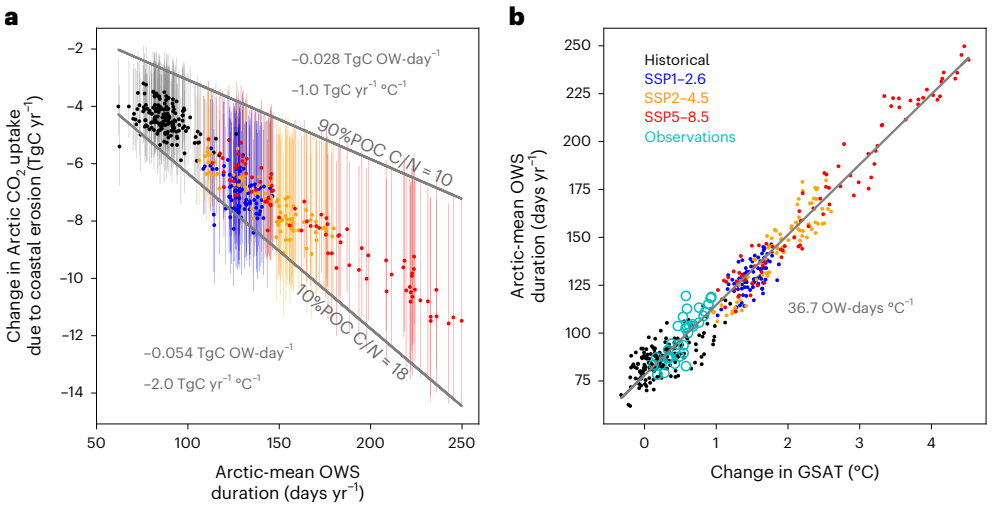

Fig. 5 | ΔCO_2 uptake sensitivities to open-water season duration and global temperature. a, Changes in CO_2 uptake due to erosion as a function of the Arctic-mean OWS duration. **b**, Changes in the OWS duration as a function of the GSAT anomalies with respect to the historical period (1850–1900). Observations in **b** are HadCRUT5 (ref. 71) for GSAT and daily sea-ice concentration from EUMETSAT OSI SAF[72] for the OWS duration. Each dot represents a year and the vertical bars in **a** express the uncertainty due to the representation of permafrost OM characteristics. Extreme OM characteristics are highlighted as linear fits in grey (slopes in **a**). Negative values in the vertical axes indicate reduced CO_2 uptake in the Inner Arctic Ocean.

POC C/N = 10 and 10% POC C/N = 18, respectively (Fig. 5a). Differences in sensitivities among emission scenarios are comparably negligible.

Since the Arctic-mean OWS duration also responds linearly to global-mean surface air temperatures (GSAT, Fig. 5b), we can express sensitivities directly in terms of GSAT. Coastal permafrost erosion would reduce the Arctic Ocean CO_2 uptake from the atmosphere by between 1 and 2 TgC yr^{-1} $°C^{-1}$ of increase in GSAT. This translates to a radiative feedback strength of ~10^{-3} W m^{-2} $°C^{-1}$, if one accumulates yearly increases in atmospheric CO_2 due to coastal erosion over 100 years (see Methods). The large range of uncertainties (factor of two in 1–2 TgC yr^{-1} $°C^{-1}$) again underlines the impact of how permafrost OM is represented in our model.

The relationship between sea ice and coastal erosion is therefore manifold. First, sea ice protects the coastal permafrost from erosion itself. The dependence of coastal erosion on open water is well documented[4–6] and is implemented in the coastal erosion model used in this study[21]. Second, sea ice determines the impact of coastal permafrost erosion on atmospheric CO_2 concentrations, by allowing the increase in surface pCO_2 to reduce the oceanic CO_2 uptake. These two factors combined explain the linear relationship we present between CO_2 uptake change and OWS duration (Fig. 5a). Third, at the seasonal scale, sea ice determines the timing at which changes driven by erosion take place. Our results highlight the implications of sea-ice melt for coastal permafrost erosion and the Arctic Ocean CO_2 sink. Sea-ice-free summers are expected in the next decades[66], which will dramatically change the mean OWS state in the future[67], especially in coastal and shelf areas (see Extended Data Fig. 1). Moreover, improving the representation of sea ice in ESMs, especially land-fast and coastal sea-ice features[68], will allow for a more accurate representation of coastal permafrost erosion as well.

Conclusion

We have represented OC fluxes from coastal permafrost erosion into the Arctic Ocean in an ESM, covering historical and future climate scenarios. We used OC fluxes from erosion obtained with a fully coupled ESM, considering future changes in sea ice, ocean-surface waves and thawing temperatures[21]. This allowed us to quantify the sensitivity of the Arctic Ocean CO_2 sink to coastal erosion, and to investigate the underlying mechanisms. In our simulations, coastal permafrost erosion reduces the Arctic Ocean CO_2 uptake from the atmosphere by 2.5–5.2 TgC yr^{-1} in the historical period and by between 4.6 and 13.2 TgC yr^{-1} by the end of the century (2081–2100 mean) depending on scenario and permafrost OM characteristics. The CO_2 uptake reduction due to coastal permafrost erosion is ~10–15% of the total Inner Arctic Ocean CO_2 uptake (excluding regions of strong Atlantic influence and perennial open water, where erosion is substantially slower; see map in Fig. 1). The yearly increase in atmospheric CO_2 due to erosion by 2100 is equivalent to about half of what was emitted by fossil fuel combustion by cars in Germany in 2021, or ~10% of emissions by cars in Europe in the same year[69].

Modern ESMs used in climate projections do not represent the full range of processes of relevance to the Arctic coast. Tides, ocean-surface waves and their effect on sediment resuspension are normally neglected, as well as a detailed representation of organic matter in the ocean, with various density classes, C/N ratios and dynamic remineralization rates. Advances have been recently made in representing coastal dynamics in regional and global ocean models[43,56,70], but such level of detail has not yet been made feasible for ESMs to run at climate-relevant timescales. Here we have performed a set of sensitivity simulations, which allowed us to present ranges of uncertainties originating in the representation of permafrost OM in our model. Such uncertainties are large, making differences between future emission scenarios indistinguishable. Improved representations of permafrost–ocean interactions in ESMs are needed to constrain our uncertainties.

We have shown that the biogeochemical feedback of coastal permafrost erosion to climate is mediated by sea ice. Coastal erosion accelerates with decreasing sea-ice cover, which in turn responds to warming caused by increasing atmospheric CO_2. Decreasing sea-ice cover allows the increase in surface pCO_2 caused by erosion to reduce the ocean CO_2 uptake, increasing atmospheric CO_2. We estimated the reduction in the ocean CO_2 uptake due to erosion at 1–2 TgC yr^{-1} $°C^{-1}$ (GSAT), which translates to a climate feedback of ~10^{-3} W m^{-2} $°C^{-1}$ over 100 years. Our results allow coastal permafrost erosion to be considered in future climate projections and carbon budget assessments.

Online content

Any methods, additional references, Nature Portfolio reporting summaries, source data, extended data, supplementary information, acknowledgements, peer review information; details of author contributions and competing interests; and statements of data and code availability are available at https://doi.org/10.1038/s41558-024-02074-3.

References

1. Rantanen, M. et al. The Arctic has warmed nearly four times faster than the globe since 1979. *Commun. Earth Environ.* **3**, 168 (2022).
2. Chylek, P. et al. Annual mean Arctic amplification 1970–2020: observed and simulated by CMIP6 climate models. *Geophys. Res. Lett.* **49**, e2022GL099371 (2022).
3. Aré, F. E. Thermal abrasion of sea coasts (part I). *Polar Geogr. Geol.* **12**, 1 (1988).
4. Irrgang, A. M. et al. Drivers, dynamics and impacts of changing Arctic coasts. *Nat. Rev. Earth Environ.* **3**, 39–54 (2022).
5. Overeem, I. et al. Sea ice loss enhances wave action at the Arctic coast. *Geophys. Res. Lett.* **38**, L17503 (2011).
6. Barnhart, K. R., Overeem, I. & Anderson, R. S. The effect of changing sea ice on the physical vulnerability of Arctic coasts. *Cryosphere* **8**, 1777–1799 (2014).
7. Lantuit, H. et al. The Arctic Coastal Dynamics Database: a new classification scheme and statistics on Arctic permafrost coastlines. *Estuaries Coasts* **35**, 383–400 (2012).
8. Grigoriev, M. N., Rachold, V., Schirrmeister, L. & Hubberten, H.-W. in *The Organic Carbon Cycle in the Arctic: Present and Past* (eds Stein, R. & Macdonald, R. W.) 41–45 (Springer, 2004).
9. Wegner, C. et al. Variability in transport of terrigenous material on the shelves and the deep Arctic Ocean during the Holocene. *Polar Res.* **34**, 24964 (2015).
10. Martens, J., Wild, B., Semiletov, I., Dudarev, O. V. & Gustafsson, Ö. Circum-Arctic release of terrestrial carbon varies between regions and sources. *Nat. Commun.* **13**, 5858 (2022).
11. Raymond, P. A. et al. Flux and age of dissolved organic carbon exported to the Arctic Ocean: a carbon isotopic study of the five largest arctic rivers. *Global Biogeochem. Cycles* **21**, GB4011 (2007).
12. McClelland, J. W. et al. Particulate organic carbon and nitrogen export from major Arctic rivers. *Global Biogeochem. Cycles* **30**, 629–643 (2016).
13. Anderson, L. G., Jutterström, S., Hjalmarsson, S., Wåhlström, I. & Semiletov, I. P. Out-gassing of CO_2 from Siberian shelf seas by terrestrial organic matter decomposition. *Geophys. Res. Lett.* **36**, L20601 (2009).
14. Vonk, J. E. et al. Activation of old carbon by erosion of coastal and subsea permafrost in Arctic Siberia. *Nature* **489**, 137–140 (2012).
15. Tanski, G. et al. Rapid CO_2 release from eroding permafrost in seawater. *Geophys. Res. Lett.* **46**, 11244–11252 (2019).
16. Tanski, G. et al. Permafrost carbon and CO_2 pathways differ at contrasting coastal erosion sites in the Canadian Arctic. *Front. Earth Sci.* https://doi.org/10.3389/feart.2021.630493 (2021).
17. Jones, B. M. et al. Increase in the rate and uniformity of coastline erosion in Arctic Alaska. *Geophys. Res. Lett.* **36**, L03503 (2009).
18. Günther, F. et al. Observing Muostakh disappear: permafrost thaw subsidence and erosion of a ground-ice-rich island in response to arctic summer warming and sea ice reduction. *Cryosphere* **9**, 151–178 (2015).
19. Irrgang, A. M. et al. Variability in rates of coastal change along the Yukon coast, 1951 to 2015. *J. Geophys. Res. Earth Surf.* **123**, 779–800 (2018).
20. Jones B. M. et al. *Coastal Permafrost Erosion* (NOAA, 2020).
21. Nielsen, D. M. et al. Increase in Arctic coastal erosion and its sensitivity to warming in the twenty-first century. *Nat. Clim. Change* **12**, 263–270 (2022).
22. Mauritsen, T. et al. Developments in the MPI-M earth system model version 1.2 (MPI-ESM1.2) and its response to increasing CO_2. *J. Adv. Model. Earth Syst.* **11**, 998–1038 (2019).
23. Dai, M. et al. Carbon fluxes in the coastal ocean: synthesis, boundary processes, and future trends. *Annu. Rev. Earth Planet. Sci.* **50**, 593–626 (2022).
24. Laruelle, G. G., Lauerwald, R., Pfeil, B. & Regnier, P. Regionalized global budget of the CO_2 exchange at the air–water interface in continental shelf seas. *Glob. Biogeochem. Cycles* **28**, 1199–1214 (2014).
25. Terhaar, J., Lauerwald, R., Regnier, P., Gruber, N. & Bopp, L. Around one third of current Arctic Ocean primary production sustained by rivers and coastal erosion. *Nat. Commun.* **12**, 169 (2021).
26. Vonk, J. E. et al. Preferential burial of permafrost-derived organic carbon in Siberian-Arctic shelf waters. *J. Geophys. Res. Oceans* **119**, 8410–8421 (2014).
27. Bröder, L., Tesi, T., Andersson, A., Semiletov, I. & Gustafsson, Ö. Bounding cross-shelf transport time and degradation in Siberian-Arctic land–ocean carbon transfer. *Nat. Commun.* **9**, 806 (2018).
28. Jong, D. et al. Nearshore zone dynamics determine pathway of organic carbon from eroding permafrost coasts. *Geophys. Res. Lett.* **47**, e2020GL088561 (2020).
29. Tesi, T., Semiletov, I., Dudarev, O., Andersson, A. & Gustafsson, Ö. Matrix association effects on hydrodynamic sorting and degradation of terrestrial organic matter during cross-shelf transport in the Laptev and east Siberian shelf seas. *J. Geophys. Res. Biogeosci.* **121**, 731–752 (2016).
30. Martens, J. et al. Stabilization of mineral-associated organic carbon in Pleistocene permafrost. *Nat. Commun.* **14**, 2120 (2023).
31. Lannuzel, D. et al. The future of Arctic sea-ice biogeochemistry and ice-associated ecosystems. *Nat. Clim. Change* **10**, 983–992 (2020).
32. Cai, W.-J. et al. Decrease in the CO_2 uptake capacity in an ice-free Arctic Ocean basin. *Science* **329**, 556–559 (2010).
33. O'Neill, B. C. et al. The scenario model intercomparison project (ScenarioMIP) for CMIP6. *Geosci. Model Dev.* **9**, 3461–3482 (2016).
34. Eyring, V. et al. Overview of the coupled model intercomparison project phase 6 (CMIP6) experimental design and organization. *Geosci. Model Dev.* **9**, 1937–1958 (2016).
35. Vonk, J. E. & Gustafsson, Ö. Permafrost-carbon complexities. *Nat. Geosci.* **6**, 675–676 (2013).
36. Turetsky, M. R. et al. Permafrost collapse is accelerating carbon release. *Nature* **569**, 32–34 (2019).
37. Turetsky, M. R. et al. Carbon release through abrupt permafrost thaw. *Nat. Geosci.* **13**, 138–143 (2020).
38. Ouyang, Z. et al. Sea-ice loss amplifies summertime decadal CO_2 increase in the western Arctic Ocean. *Nat. Clim. Change* **10**, 678–684 (2020).
39. Vonk, J. E. et al. High biolability of ancient permafrost carbon upon thaw. *Geophys. Res. Lett.* **40**, 2689–2693 (2013).
40. Sánchez-García, L. et al. Inventories and behavior of particulate organic carbon in the Laptev and east Siberian seas. *Global Biogeochem. Cycles* **25**, GB2007 (2011).
41. Alling, V. et al. Nonconservative behavior of dissolved organic carbon across the Laptev and east Siberian seas. *Global Biogeochem. Cycles* **24**, GB4033 (2010).
42. Maerz, J., Six, K. D., Stemmler, I., Ahmerkamp, S. & Ilyina, T. Microstructure and composition of marine aggregates as co-determinants for vertical particulate organic carbon transfer in the global ocean. *Biogeosciences* **17**, 1765–1803 (2020).
43. Mathis, M. et al. Seamless integration of the coastal ocean in global marine carbon cycle modeling. *J. Adv. Model. Earth Syst.* **14**, e2021MS002789 (2022).
44. Ilyina, T. et al. Global ocean biogeochemistry model HAMOCC: model architecture and performance as component of the MPI-Earth system model in different CMIP5 experimental realizations. *J. Adv. Model. Earth Syst.* **5**, 287–315 (2013).
45. Humborg, C. et al. Sea–air exchange patterns along the central and outer east Siberian Arctic shelf as inferred from continuous CO_2, stable isotope, and bulk chemistry measurements. *Global Biogeochem. Cycles* **31**, 1173–1191 (2017).

46. Semiletov, I. P., Pipko, I. I., Repina, I. & Shakhova, N. E. Carbonate chemistry dynamics and carbon dioxide fluxes across the atmosphere–ice–water interfaces in the Arctic Ocean: Pacific sector of the Arctic. *J. Mar. Syst.* **66**, 204–226 (2007).
47. Pipko, I. I., Semiletov, I. P., Tishchenko, P. Y., Pugach, S. P. & Savel'eva, N. I. Variability of the carbonate system parameters in the coast-shelf zone of the east Siberian Sea during the autumn season. *Oceanology* **48**, 54–67 (2008).
48. Pipko, I. I., Semiletov, I. P., Pugach, S. P., Wåhlström, I. & Anderson, L. G. Interannual variability of air-sea CO_2 fluxes and carbon system in the east Siberian Sea. *Biogeosciences* **8**, 1987–2007 (2011).
49. Semiletov, I. P., Shakhova, N. E., Sergienko, V. I., Pipko, I. I. & Dudarev, O. V. On carbon transport and fate in the east Siberian Arctic land–shelf–atmosphere system. *Environ. Res. Lett.* **7**, 015201 (2012).
50. Semiletov, I. P. et al. Acidification of east Siberian Arctic shelf waters through addition of freshwater and terrestrial carbon. *Nat. Geosci.* **9**, 361–365 (2016).
51. Semiletov, I. P. Destruction of the coastal permafrost as an important factor in biogeochemistry of the Arctic shelf waters. *Dokl. Akad. Nauk* **368**, 679–682 (1999).
52. Manizza, M. et al. A model of the Arctic Ocean carbon cycle. *J. Geophys. Res. Oceans* **116**, C12020 (2011).
53. Wåhlström, I., Omstedt, A., Björk, G. & Anderson, L. G. Modeling the CO_2 dynamics in the Laptev sea, Arctic Ocean: part II. Sensitivity of fluxes to changes in the forcing. *J. Mar. Syst.* **111**, 1–10 (2013).
54. Terhaar, J., Orr, J. C., Ethé, C., Regnier, P. & Bopp, L. Simulated Arctic Ocean response to doubling of riverine carbon and nutrient delivery. *Global Biogeochem. Cycles* **33**, 1048–1070 (2019).
55. Lacroix, F., Ilyina, T. & Hartmann, J. Oceanic CO_2 outgassing and biological production hotspots induced by pre-industrial river loads of nutrients and carbon in a global modeling approach. *Biogeosciences* **17**, 55–88 (2020).
56. Bertin, C. et al. Biogeochemical river runoff drives intense coastal Arctic Ocean CO_2 outgassing. *Geophys. Res. Lett.* **50**, e2022GL102377 (2023).
57. Forest, A. et al. Synoptic evaluation of carbon cycling in the Beaufort Sea during summer: contrasting river inputs, ecosystem metabolism and air–sea CO_2 fluxes. *Biogeosciences* **11**, 2827–2856 (2014).
58. Landschützer, P. et al. An Updated Observation-based Global Monthly Gridded Sea Surface pCO_2 and Air–Sea CO_2 Flux Product from 1982 through 2015 and its Monthly Climatology (National Centers for Environmental Information, 2017).
59. Roobaert, A. et al. The spatiotemporal dynamics of the sources and sinks of CO_2 in the global coastal ocean. *Global Biogeochem. Cycles* **33**, 1693–1714 (2019).
60. Orr, J. C., Kwiatkowski, L. & Pörtner, H.-O. Arctic Ocean annual high in pCO_2 could shift from winter to summer. *Nature* **610**, 94–100 (2022).
61. Ardyna, M. & Arrigo, K. R. Phytoplankton dynamics in a changing Arctic Ocean. *Nat. Clim. Change* **10**, 892–903 (2020).
62. Bates, N. R. & Mathis, J. T. The Arctic Ocean marine carbon cycle: evaluation of air–sea CO_2 exchanges, ocean acidification impacts and potential feedbacks. *Biogeosciences* **6**, 2433–2459 (2009).
63. Yamamoto-Kawai, M., McLaughlin, F. A., Carmack, E. C., Nishino, S. & Shimada, K. Aragonite undersaturation in the Arctic Ocean: effects of ocean acidification and sea ice melt. *Science* **326**, 1098–1100 (2009).
64. Prytherch, J. et al. Direct determination of the air–sea CO_2 gas transfer velocity in Arctic sea ice regions. *Geophys. Res. Lett.* **44**, 3770–3778 (2017).
65. Butterworth, B. J. & Miller, S. D. Air–sea exchange of carbon dioxide in the Southern Ocean and Antarctic marginal ice zone. *Geophys. Res. Lett.* **43**, 7223–7230 (2016).
66. Notz, D. & SIMIP Community. Arctic sea ice in CMIP6. *Geophys. Res. Lett.* **47**, e2019GL086749 (2020).
67. Crawford, A., Stroeve, J., Smith, A. & Jahn, A. Arctic open-water periods are projected to lengthen dramatically by 2100. *Commun. Earth Environ.* **2**, 109 (2021).
68. Hošeková, L. et al. Landfast ice and coastal wave exposure in northern Alaska. *Geophys. Res. Lett.* **48**, e2021GL095103 (2021).
69. European Environment Agency *Greenhouse Gas Emissions By Source Sector* https://ec.europa.eu/eurostat/databrowser/bookmark/df121a5f-2a95-4b26-aeb9-c687f9dd3162?lang=en (2023).
70. Mathis, M. et al. Enhanced CO_2 uptake of the coastal ocean is dominated by biological carbon fixation. *Nat. Clim. Change* **14**, 373–379 (2024).
71. Morice, C. P. et al. An updated assessment of near-surface temperature change from 1850: the HadCRUT5 data set. *J. Geophys. Res. Atmos.* **126**, e2019JD032361 (2021).
72. Lavergne, T. et al. Version 2 of the EUMETSAT OSI SAF and ESA CCI sea-ice concentration climate data records. *Cryosphere* **13**, 49–78 (2019).

Publisher's note Springer Nature remains neutral with regard to jurisdictional claims in published maps and institutional affiliations.

Open Access This article is licensed under a Creative Commons Attribution 4.0 International License, which permits use, sharing, adaptation, distribution and reproduction in any medium or format, as long as you give appropriate credit to the original author(s) and the source, provide a link to the Creative Commons licence, and indicate if changes were made. The images or other third party material in this article are included in the article's Creative Commons licence, unless indicated otherwise in a credit line to the material. If material is not included in the article's Creative Commons licence and your intended use is not permitted by statutory regulation or exceeds the permitted use, you will need to obtain permission directly from the copyright holder. To view a copy of this licence, visit http://creativecommons.org/licenses/by/4.0/.

© The Author(s) 2024

Methods

Earth system model

We used the MPI-ESM[22] in the same version (1.2) and configuration used for the Coupled Model Intercomparison Project phase 6 (CMIP6)[33]. The atmospheric component of MPI-ESM is the European Center-Hamburg model (ECHAM6)[73], configured with T63 horizontal resolution (~1.875° on a Gaussian grid) and 47 unevenly spaced vertical levels. The land-surface, dynamic-vegetation model JSBACH[74] is embedded in the atmospheric component. The ocean component of MPI-ESM is the Max Planck Institute Ocean Model (MPIOM)[75], a free-surface ocean general circulation model on an Arakawa-C grid with nominal 1.5° horizontal resolution. This configuration of MPIOM uses two poles, one in Greenland and another in Antarctica. In the Arctic Ocean, MPIOM has horizontal resolution ranging between 20 km and 100 km. MPIOM uses *z*-vertical coordinates in 40 unevenly spaced layers. Ocean and atmosphere are coupled daily without flux adjustments by the Ocean Atmosphere Sea Ice Soil (OASIS3) coupler[76]. Ocean biogeochemistry is simulated by the Hamburg Ocean Carbon Cycle model (HAMOCC)[44,77].

HAMOCC represents biogeochemical cycles in the water column, interactions with the atmosphere and in the sediment. Marine biology in HAMOCC is based on an extended NPDZ (nutrients, phytoplankton, zooplankton and detritus) approach for OM production and remineralization. Primary production in HAMOCC is represented by two variables, namely, bulk phytoplankton (algae, among them calcifying and silicifying species) and cyanobacteria. Growth of bulk phytoplankton and cyanobacteria is limited by light and the least available nutrient (nitrate, phosphate and iron), except that cyanobacteria can utilize dinitrogen instead of nitrate (nitrogen fixation). In the standard HAMOCC setup, particulate organic carbon (POC) represents the carbon pool of non-living OM formed by dead primary producers and zooplankton, and zooplankton faecal pellets. Dissolved organic carbon (DOC) represents the carbon pool of non-living OM formed by exudation of primary producers and zooplankton excretion. Here we extend the definitions of POC and DOC to account for the effect of coastal permafrost erosion (see next section 'Representing coastal permafrost erosion in MPI-ESM'). POC is transported downwards by gravitational sinking at constant speed (3.5 m day^{-1}) in the first 100 m, and linearly increasing speed with depth afterwards, resulting in a power-law profile of concentrations and fluxes (Martin curve[78]). DOC is transported in all directions by advection and parameterized mixing but does not sink. In this version of HAMOCC, remineralization rates for POC and DOC are globally constant at 2.6×10^{-2} and 8.0×10^{-3} day^{-1}, respectively. All organic matter in HAMOCC has fixed stoichiometry of C:N:P:O_2:Fe = 122:16:1:−172:366×10^{-6} following the Redfield ratio concept[79], which is modified for permafrost OM (see next).

Representing coastal permafrost erosion in MPI-ESM

We modified MPI-ESM to include OM fluxes from coastal permafrost erosion into the ocean by prescribing them in HAMOCC. We performed simulations with varying characteristics of permafrost OM, namely, the fraction of OC flux represented as POC and DOC (here accounting for the neutrally buoyant and passively transported POC), and the OM carbon-nutrient ratio (C/N). This allowed us to encompass varying characteristics observed in permafrost OM and, at the same time, provide a range of uncertainties originating in the parameterization of such characteristics. Such permafrost OM characteristics determine the balance between remineralization and photosynthesis in our model, which together drive changes in surface pCO_2 and, ultimately, in air–sea CO_2 fluxes. OM remineralization increases surface DIC and decreases alkalinity, both contributing to increase in surface pCO_2. Conversely, primary production decreases surface DIC and increases alkalinity, both decreasing surface pCO_2. On the one hand, prolonging the lifetime of OM in the water column allows for more OM remineralization, which is achieved by increasing the fraction of the OM represented as passively transported and non-sinking POC, as opposed to sinking POC. On the other hand, increasing the nutrient content of permafrost OM allows for a larger boost in primary production, which is achieved by representing permafrost OM with low C/N ratios.

Observations show that most of the OM mobilized by coastal permafrost erosion is in the form of POC, as opposed to DOC[80,81]. However, much of the POC delivered by erosion is of low density[29,82]. Here we made use of HAMOCC's POC and DOC tracer properties of sinking and being neutrally buoyant, respectively. We thus transport the eroded permafrost OM as both POC and DOC (adjusted for permafrost) in HAMOCC. This combination allows us to represent both the sinking POC and the neutrally buoyant POC delivered by erosion. Therefore, we performed simulations with either 10% POC (and 90% DOC) or 90% POC (and 10% DOC). Our extreme 10–90% and 90–10% POC–DOC partitioning serves two purposes:

First, a large fraction of the POC from erosion in coastal areas was observed to be of low density[29,82] and thus relatively long-lived in the water column. Reference 82 recently showed that between <2% and 15% of the OC sampled on land and in the water column around Herschel Island (Canadian Beaufort Sea) is classified as 'low density', the least abundant fraction in weight. However, their low-density fraction is also by far the most abundant fraction in OC, with 22 ± 5% of OC content. They reported the low-density fraction to be composed of relatively fresh and matrix-free debris, probably originating in relatively young Holocene-aged permafrost. It is thus clear that we must represent a fraction of the eroded OM with relatively low density, and we must do this while bounded by MPI-ESM limitations. Since all POC in HAMOCC is assumed to be of high density and sinks, our low-POC (and high-DOC) simulations allowed us to account for the low-density, slowly sinking POC fraction from erosion.

Second, sediment resuspension at the Arctic coast is mainly forced by vertical mixing driven by wind ocean-surface waves and tides. However, MPI-ESM does not directly represent ocean-surface waves, hence sediment resuspension is under-represented in the Arctic. This is not a deficiency of MPI-ESM in particular and, to the best of our knowledge, no CMIP6 ESM includes the representation of ocean-surface waves and their effect on sediment resuspension. For this reason, we used the sinking properties of POC and DOC in HAMOCC (that is, sinking and neutrally buoyant, respectively), and divided the OM delivered by erosion between POC and DOC in sensitivity experiments with 90%–10% and 10%–90% proportions. Our low-POC (and high-DOC) simulations avoid excessive OM sinking and burial into the sediment, thus mimicking a prolonged OM lifetime in the water column by recurrent resuspension–deposition cycles that can take place in shelf regions.

In summary, the DOC delivered by erosion in our experiments represents the neutrally buoyant POC fraction of the eroded OM and the indirect effect of repeated resuspension–deposition cycles. In addition, typical water residence times over the Arctic shelves are relatively long (order of years to decades[83,84]), which exceeds POC remineralization timescales. Our results indicate little effect of this treatment outside the Arctic shelves, further justifying this approach. Therefore, our experiments were designed to cover a wide range of transport behaviours of eroded POC. We discuss in detail the implications of our modelling strategy in comparison with observations in Supplementary Information (see 'POC export and sediment fluxes' and 'POC vs DOC in the water column').

We performed simulations with fixed permafrost OM C/N values of 10, 14 and 18 (total carbon to total nitrogen ratios). The range in C/N ratios used here approximates the mean and one standard deviation of values reported in the literature across the Arctic permafrost[16,51,85–92]. The excess carbon with respect to the stoichiometric ratio fixed in HAMOCC is given to the ocean as DIC, which assumes a fraction of instantaneous remineralization upon erosion while not changing alkalinity. We also performed a reference simulation configured as one ensemble member from the MPI-ESM-LR contribution to CMIP6 (ref. 33,93), which produces identical physics output (ocean and

atmosphere) as our modified simulations with coastal permafrost erosion. A summary of the sensitivity experiments performed here is presented in Table 1.

Each experiment was performed covering the historical period (1850–2014) and three future scenarios (2015–2100) from CMIP6 (ref. 34). The future scenarios cover a wide range of societal pathways and, consequently, atmospheric CO_2 concentrations and greenhouse-gas (GHG) radiative forcings, namely: (1) SSP1–2.6: low end-of-century GHG forcing due to strong societal shifts towards sustainable practices; (2) SSP2–4.5: intermediate GHG forcing, no strong shifts, the 'middle of the road'; and (3) SSP5–8.5: strong GHG forcing, energy-intensive and fossil fuel-based growing economy[33].

Coastal erosion OM fluxes

We considered the historical and future OC flux projections of ref. 21, which combine sea ice and temperatures from MPI-ESM and surface-ocean wave simulations, with ground-ice, OC and coastal-segment dimensions from the Arctic Coastal Dynamics (ACD) database[7] in a simple, semi-empirical model for coastal erosion. The here-considered present-climate pan-Arctic OC flux is 8.5 (3.3–13.7) TgC yr^{-1} (ref. 21), which is within the range of previous estimates (6.7 TgC yr^{-1} (ref. 8); 4.9–14 TgC yr^{-1} (ref. 9)). More recently, ref. 10 estimated the OC flux from the ice-complex deposits (Yedoma) at 13.4 (8.8–18.0) TgC yr^{-1}, which would mainly represent coastal erosion, based on an extensive compilation of observations from the Arctic shelves (CASCADE)[94]. Their recent estimate is larger than our present-climate range and stands closer to our end-of-the-century range for SSP2–4.5 (13.0 ± 3.3 TgC yr^{-1} (ref. 21)). In this context, our results would be rather conservative in absolute terms. By the end-of-the century, the here-considered OC fluxes are 11.4 (5.9–16.8) TgC yr^{-1} and 17.2 (9.0–25.4) TgC yr^{-1} for SSP1–2.6 and SSP5–8.5, respectively[21].

We distributed yearly fluxes to daily resolution using normalized means of daily curves positive surface air temperatures and ocean-surface waves every year, which are limited to the open-water season at each ocean grid cell. In our version of MPI-ESM, there were no feedbacks from ocean biogeochemistry to ocean physics or atmosphere. Therefore, our daily fluxes of OM from erosion were prescribed to the identical physical state that was used to generate them. That is, we guaranteed that erosion fluxes are locally limited to sea-ice-free conditions and match their local forcings (peaks in thawing temperatures and storms) every year. Except for the inclusion of coastal permafrost erosion OM fluxes, our MPI-ESM simulations were configured identically to those produced for CMIP6, with prescribed CO_2 concentrations in the atmosphere.

Decomposing ΔpCO_2 between DIC and alkalinity

Surface pCO_2 is a function of DIC concentration, alkalinity, temperature and salinity. In the current version of MPI-ESM, changes in ocean biogeochemistry, such as those driven by erosion, do not feedback to the ocean physics or atmosphere. That is, temperature and salinity are identical among simulations with and without erosion. Following ref. 79, we decomposed the total change in pCO_2 due to erosion ($\Delta pCO_{2,Total}$) between contributions from changes in DIC due to erosion (ΔDIC) and changes in alkalinity due to erosion (ΔAlk):

$$\Delta pCO_{2,Total} = \Delta DIC \frac{\partial pCO_2}{\partial DIC} + \Delta Alk \frac{\partial pCO_2}{\partial Alk} \quad (1)$$

The sensitivity parameters of pCO_2 to DIC and alkalinity, γ_{DIC} and γ_{Alk} respectively, are:

$$\gamma_{DIC} = \frac{\partial pCO_2}{\partial DIC} \frac{DIC_{Ref}}{pCO_{2,Ref}}, \text{ and}$$
$$\gamma_{Alk} = \frac{\partial pCO_2}{\partial Alk} \frac{Alk_{Ref}}{pCO_{2,Ref}}, \quad (2)$$

where $pCO_{2,Ref}$, DIC_{Ref} and Alk_{Ref} are reference values for pCO_2, DIC and alkalinity, respectively. In our case, reference values were taken from the reference CMIP6 simulation without erosion. The parameters γ_{DIC} and γ_{Alk} therefore express linear transformations from percentage changes in DIC and alkalinity due to erosion to percentage changes in pCO_2 due to erosion. Absolute changes in pCO_2 due to erosion, decomposed between contributions from percentage changes in DIC and alkalinity due to erosion, were calculated as:

$$\Delta pCO_{2,DIC} = \gamma_{DIC} \frac{\Delta DIC}{DIC_{Ref}} pCO_{2,Ref}$$
$$\Delta pCO_{2,ALK} = \gamma_{Alk} \frac{\Delta Alk}{Alk_{Ref}} pCO_{2,Ref} \quad (3)$$

We used $\gamma_{DIC} = 13.3$ and $\gamma_{Alk} = -12.6$ for high latitudes following ref. 95 in equation (3) to calculate the ΔpCO_2 components. With this assumption, our reconstructed $\Delta pCO_{2,Total} = \Delta pCO_{2,DIC} + \Delta pCO_{2,Alk}$ shows a bias of ~0.4 Pa on average with respect to the ΔpCO_2 simulated by MPI-ESM. Nonetheless, the bias is constant in time in all sensitivity simulations and scenarios. Therefore, this method suffices to allow us to explore qualitatively the relative contributions of DIC and alkalinity to ΔpCO2, especially in terms of whether contributions are positive or negative.

Estimating sensitivity coefficients

The sensitivity of CO_2 uptake change to erosion OC flux (Fig. 1e), the sensitivity of CO_2 uptake change to OWS duration (Fig. 5a) and the sensitivity of OWS duration to GSAT (Fig. 5b) were calculated as linear regressions, taking annual time series as input. We did not detrend time series before regression, as we were interested in the long-term response of the dependent variable to the regressor, instead of the interannual response. Uncertainties displayed are the 5–95th percentile range obtained with a bootstrapping method (that is, by obtaining a distribution of coefficient estimates by sampling with replacement) in Fig. 1e. However, in Fig. 5, the vertical bars depict the range obtained by varying permafrost OM characteristics among sensitivity experiments.

Estimating the erosion–climate feedback

We estimated the feedback of coastal permafrost erosion to climate based on a simple approach. Using our 1–2 TgC yr^{-1} °C^{-1} estimate and accumulating emissions over 100 years (following the typical timescale used by the IPCC for future projections[96]), coastal permafrost erosion would release 0.1–0.2 PgC to the atmosphere as CO_2. This translates to 0.05–0.1 ppm increase in atmospheric CO_2, assuming 2.12 ppm PgC^{-1} and neglecting any land uptake. We calculated the additional radiative forcing, ΔF, caused by coastal permafrost erosion using $\Delta F = 5.35 \ln(1 + C_{eros}/C_0)$, where $C_0 = 400$ ppm is the modern atmospheric CO_2 concentration and C_{eros} is the added atmospheric CO_2 by coastal permafrost erosion over 100 years per degree of increase in GSAT, in ppm. We find that the feedback $\lambda = \Delta F/\Delta T = 0.0009–0.001 \approx 10^{-3}$ W m^{-2} °C^{-1}. Although this is a small number, it is certainly positive, and it should add to the highly uncertain biogeophysical and biogeochemical feedbacks assessed by IPCC[96]. Of note, the assumed timescale for CO_2 accumulation greatly impacts the magnitude of the feedback. As the lifetime of anthropogenic CO_2 in the atmosphere is multicentennial[97], this is a rather conservative estimate.

Data availability

MPI-ESM historical and scenario CMIP6 experiment outputs are publicly available for download from the ESGF website at https://doi.org/10.22033/ESGF/CMIP6.793. MPI-ESM post-processed experiment outputs including coastal permafrost erosion are publicly available at the World Data Center for Climate (WDCD)/Deutsche Klimarechenzentrum (DKRZ)[98]. All maps were made using Natural Earth data (https://www.naturalearthdata.com) with Cartopy[99].

Code availability

The CMIP6 version of the MPI-ESM code is publicly available at https://doi.org/10.17617/3.H44EN5 (ref. 100). The modified MPI-ESM code including OM fluxes from coastal permafrost erosion is publicly available at WDCD/DKRZ[101]. The scripts to reproduce figures are also publicly available at the World Data Center for Climate WDCD/ DKRZ[98].

References

73. Stevens, B. et al. Atmospheric component of the MPI-M earth system model: ECHAM6. *J. Adv. Model. Earth Syst.* **5**, 146–172 (2013).
74. Reick, C. H., Raddatz, T., Brovkin, V. & Gayler, V. Representation of natural and anthropogenic land cover change in MPI-ESM. *J. Adv. Model. Earth Syst.* **5**, 459–482 (2013).
75. Jungclaus, J. H. et al. Characteristics of the ocean simulations in the Max Planck Institute ocean model (MPIOM) the ocean component of the MPI-Earth system model. *J. Adv. Model. Earth Syst.* **5**, 422–446 (2013).
76. Valcke, S. The OASIS3 coupler: a European climate modelling community software. *Geosci. Model Dev.* **6**, 373–388 (2013).
77. Paulsen, H., Ilyina, T., Six, K. D. & Stemmler, I. Incorporating a prognostic representation of marine nitrogen fixers into the global ocean biogeochemical model HAMOCC. *J. Adv. Model. Earth Syst.* **9**, 438–464 (2017).
78. Martin, J. H., Knauer, G. A., Karl, D. M. & Broenkow, W. W. VERTEX: carbon cycling in the northeast Pacific. *Deep Sea Res. A Oceanogr. Res. Pap.* **34**, 267–285 (1987).
79. Takahashi, T., Olafsson, J., Goddard, J. G., Chipman, D. W. & Sutherland, S. C. Seasonal variation of CO_2 and nutrients in the high-latitude surface oceans: a comparative study. *Global Biogeochem. Cycles* **7**, 843–878 (1993).
80. Tanski, G., Couture, N., Lantuit, H., Eulenburg, A. & Fritz, M. Eroding permafrost coasts release low amounts of dissolved organic carbon (DOC) from ground ice into the nearshore zone of the Arctic Ocean. *Global Biogeochem. Cycles* **30**, 1054–1068 (2016).
81. Guo, L., Ping, C.-L. & Macdonald, R. W. Mobilization pathways of organic carbon from permafrost to Arctic rivers in a changing climate. *Geophys. Res. Lett.* **34**, GL030689 (2007).
82. Jong, D. et al. Selective sorting and degradation of permafrost organic matter in the nearshore zone of Herschel Island (Yukon, Canada). *J. Geophys. Res. Biogeosci.* **129**, e2023JG007479 (2024).
83. Sharples, J., Middelburg, J. J., Fennel, K. & Jickells, T. D. What proportion of riverine nutrients reaches the open ocean? *Global Biogeochem. Cycles* **31**, 39–58 (2017).
84. Lacroix, F., Ilyina, T., Laruelle, G. G. & Regnier, P. Reconstructing the preindustrial coastal carbon cycle through a global ocean circulation model: was the global continental shelf already both autotrophic and a CO_2 sink? *Global Biogeochem. Cycles* **35**, e2020GB006603 (2021).
85. Schirrmeister, L. et al. Sedimentary characteristics and origin of the late Pleistocene ice complex on north-east Siberian Arctic coastal lowlands and islands - a review. *Quat. Int.* **241**, 3–25 (2011).
86. Couture, N. J., Irrgang, A., Pollard, W., Lantuit, H. & Fritz, M. Coastal erosion of permafrost soils along the Yukon coastal plain and fluxes of organic carbon to the Canadian Beaufort Sea. *J. Geophys. Res. Biogeosci.* **123**, 406–422 (2018).
87. Fuchs, M. et al. Carbon and nitrogen pools in thermokarst-affected permafrost landscapes in Arctic Siberia. *Biogeosciences* **15**, 953–971 (2018).
88. Jongejans, L. L. et al. Organic matter characteristics in yedoma and thermokarst deposits on Baldwin Peninsula, west Alaska. *Biogeosciences* **15**, 6033–6048 (2018).
89. Fuchs, M. et al. Organic carbon and nitrogen stocks along a thermokarst lake sequence in Arctic Alaska. *J. Geophys. Res. Biogeosci.* **124**, 1230–1247 (2019).
90. Bristol, E. M. et al. Geochemistry of coastal permafrost and erosion-driven organic matter fluxes to the Beaufort Sea near Drew Point, Alaska. *Front. Earth Sci.* https://doi.org/10.3389/feart.2020.598933 (2021).
91. Fuchs, M. et al. Rapid fluvio-thermal erosion of a yedoma permafrost cliff in the Lena River delta. *Front. Earth Sci.* https://doi.org/10.3389/feart.2020.00336 (2020).
92. Wetterich, S. et al. The cryostratigraphy of the Yedoma cliff of Sobo-Sise Island (Lena delta) reveals permafrost dynamics in the central Laptev Sea coastal region during the last 52 kyr. *Cryosphere* **14**, 4525–4551 (2020).
93. Wieners, K.-H. et al. MPI-M MPIESM1.2-LR model output prepared for CMIP6 ScenarioMIP ssp585. *scite* https://doi.org/10.22033/esgf/cmip6.6705 (2019).
94. Martens, J. et al. Cascade – the circum-Arctic sediment carbon database. *Earth Syst. Sci. Data* **13**, 2561–2572 (2021).
95. Sarmiento, J. L. & Gruber, N. *Ocean Biogeochemical Dynamics* (Princeton Univ. Press, 2006).
96. Forster, P. et al. in *Climate Change 2021: The Physical Science Basis* (eds Masson-Delmotte, V. et al.) 923–1054 (Cambridge Univ. Press, 2021).
97. Archer, D. & Brovkin, V. The millennial atmospheric lifetime of anthropogenic CO_2. *Clim. Change* **90**, 283–297 (2008).
98. Nielsen, D. M. et al. MPI-ESM model output including coastal permafrost erosion and plotting scripts. *DOKU at DKRZ* https://hdl.handle.net/21.14106/168ba7cba84d3de51ffb9a6d4507e55891846e30 (2024).
99. Cartopy: A Cartographic Python Library with a Matplotlib Interface (Met Office, 2010).
100. MPI-ESM 1.2.01p7 (Model Development Team Max-Planck-Institut für Meterologie, 2024).
101. Nielsen, D. M. et al. Modified MPI-ESM model code including coastal permafrost erosion. *DOKU at DKRZ* https://hdl.handle.net/21.14106/f81e2d7ca6141bbf7ec4c75c52830463f8f93154 (2024).

Acknowledgements

D.M.N., J.M., M.M., J.B., V.B. and T.I. are funded by the Deutsche Forschungsgemeinschaft (DFG, German Research Foundation) under Germany's Excellence Strategy - EXC 2037 'CLICCS - Climate, Climatic Change, and Society' - project no. 390683824, contribution to the Center for Earth System Research and Sustainability (CEN) of Universität Hamburg, and to the Max Planck Institute of Meteorology. J.B. and S.B. were supported by Copernicus Climate Change Service, funded by the EU, under contract C3S2-370. D.M.N., F.C., M.D., T.I. and V.B. are funded by EU Horizon 2020 research and innovation programme under grant agreement no. 773421 - project 'Nunataryuk'. F.C., J.M. and T.I. are funded by the EU Horizon 2020 research and innovation programme under grant agreement no. 101003536 (ESM2025-Earth System Models for the Future). We thank M. Ritschel for help with sea-ice observations.

Author contributions

D.M.N., M.D., J.B., V.B. and T.I. conceived the study idea and designed the experiments. F.C. and J.M. modified the MPI-ESM code, while D.M.N. performed the model simulations. D.M.N. performed the data analyses. All co-authors contributed to analysing the results and deriving conclusions. D.M.N. wrote the manuscript, with contributions from all co-authors.

Funding

Open access funding provided by Max Planck Society.

Competing interests
The authors declare no competing interests.

Additional information
Extended data is available for this paper at https://doi.org/10.1038/s41558-024-02074-3.

Supplementary information The online version contains supplementary material available at https://doi.org/10.1038/s41558-024-02074-3.

Correspondence and requests for materials should be addressed to David M. Nielsen.

Peer review information *Nature Climate Change* thanks Manfredi Manizza, Dustin Whalen and the other, anonymous, reviewer(s) for their contribution to the peer review of this work.

Reprints and permissions information is available at www.nature.com/reprints.

https://doi.org/10.1038/s41558-024-02074-3

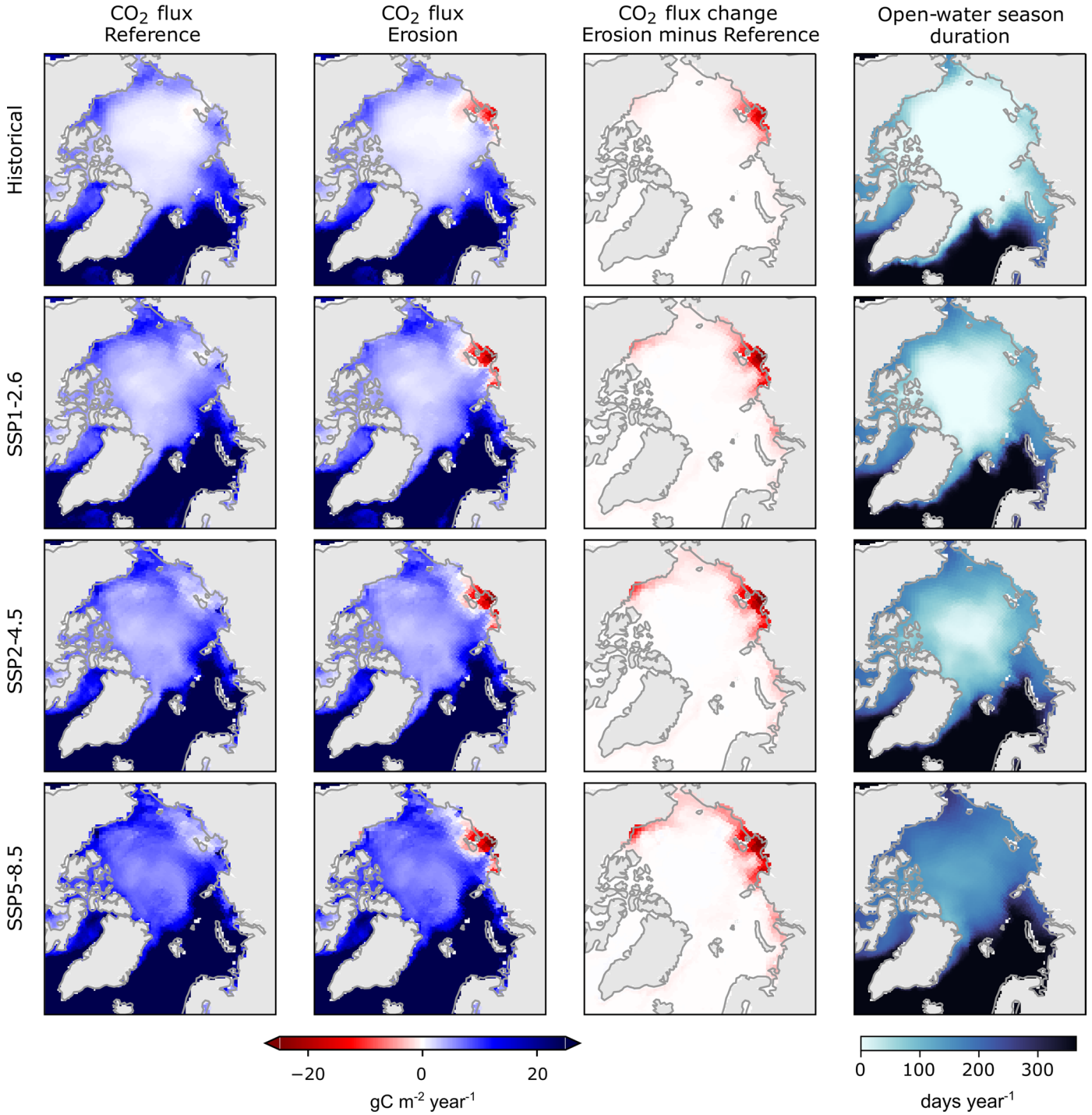

Extended Data Fig. 1 | Air-sea CO_2 flux and open-water season (OWS) duration. Historical (1850-1900) and end-of-the-century scenario (2081-2100) means of: air-sea CO_2 flux in the CMIP6 reference without erosion (first column), in the mean of all six simulations with coastal permafrost OM erosion (second column), the difference between the two (that is erosion minus reference, third column), and the concurrent duration of the OWS (fourth column). For air-sea CO_2 fluxes, positive values mean ocean uptake (blue, downward flux), while negative values mean ocean outgassing (red, upward flux).

https://doi.org/10.1038/s41558-024-02074-3

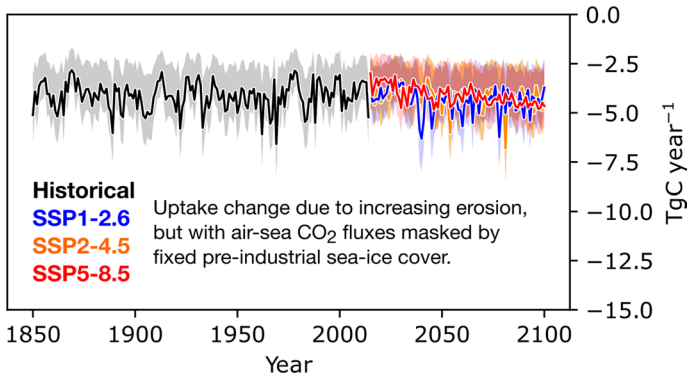

Extended Data Fig. 2 | Arctic Ocean CO_2 uptake reduction scaled with fixed sea ice. Change in Arctic Ocean CO_2 uptake due to erosion (that is, simulations with erosion minus simulations without erosion), as in Fig. 1a in the main text. However, here, we estimate changes in the Arctic Ocean CO_2 uptake due to erosion, if sea-ice cover were fixed at pre-industrial (1850-1900) extent. This estimates the maximum effect of sea ice at mediating air-sea CO_2 fluxes, while neglecting the effect of the seasonal redistribution of pCO_2 and potentially increasing CO_2 fluxes within a shorter open-water season. By doing so, the impact of erosion on the CO_2 uptake becomes constant in time, and about 50-60% smaller by the end of the century in comparison with our simulated CO_2 uptake reduction (Fig. 1a in the main text).